RESEARCH PAPER

CrossMark

Three-dimensional flow velocity and wall shear stress distribution measurement on a micropillar-arrayed surface using astigmatism PTV to understand the influence of microstructures on the flow field

Yoshiyasu Ichikawa[1] · Ken Yamamoto[1,2] · Masahiro Motosuke[1,2]

Abstract

In this study, the influence of the microstructure in a microchannel on the three-dimensional (3D) flow field and shear stress distribution on the wall was investigated with 3D velocity measurement method. In a micro-total analysis system or a lab-on-a-chip application, the control of the flow is necessary. Thus, microstructures are often applied to the fluidic system for passive flow control. However, the flow field which interacts with microstructures becomes complicated three-dimensionally. The 3D measurement of such microfluidic flow would give insight on the interaction of the flow with the structures and be also useful for other applications. In this study, micropillar array was introduced in a microchannel and we investigated the influence of the micropillar on the 3D flow field by the astigmatism particle tracking velocimetry which enables to determine three-dimensional and three-component velocity by single-viewing. Furthermore, the wall shear stress distribution was also investigated. From measurement results, it was confirmed that the pillar changes the wall shear stress distribution and 3D velocity distribution. Compared to a flat channel (no-pillar array), the wall shear stress in our channel varied spatially in a range of approximately -80 to $+20\%$. Moreover, we also conducted a numerical simulation to consolidate the measurement results.

Keywords Wall shear stress distribution · Astigmatism particle tracking velocimetry · 3D3C velocity measurement · Micropillar array

1 Introduction

With the drastic growth of microfluidic devices like micro-total analysis systems (μTAS) and lab-on-a-chip all over the world, precise control of the fluid motion in a microchannel has received considerable attention for biological processing (Toner and Irimia 2005), chemical reaction control (Elvira et al. 2013), and creating advanced materials (Blossey 2003). In passive microfluidic devices, flow fields are modified by a combination of channel geometry and microstructures like pillars on the surface, and correspondingly the mass and momentum transfer is altered. As well as mass and momentum transport/mixing mechanism, understanding how the fluid flow interacts with microstructures on the surface has been focused upon (Stroock et al. 2002). When the fluid flow interacts with microstructures, the flow field often becomes complex three-dimensionally (Stone et al. 2004; Amini et al. 2013; Stoecklein et al. 2014). Thus, to reveal the actual influence of the structured surface on the flow field and wall shear stress, three-dimensional (3D) flow measurement should be conducted.

The shear stress on the wall τ_w is defined as a product of viscosity and the velocity gradient at the wall, as represented in Eq. (1):

$$\tau_w = \mu \frac{\partial u}{\partial z}\big|_{z=\text{wall}}. \tag{1}$$

Here, μ is the fluid viscosity, u is the streamwise flow velocity, and z is the distance from the wall. The wall shear stress measurement is often essential and important in many fields; for example, to evaluate drag reduction effect

✉ Masahiro Motosuke
   mot@rs.tus.ac.jp

1   Department of Mechanical Engineering, Tokyo University of Science, 6-3-1, Niijuku, Katsushika-ku, Tokyo 125-8585, Japan

2   Research Institute for Science and Technology, Tokyo University of Science, 6-3-1, Niijuku, Katsushika-ku, Tokyo 125-8585, Japan

of superhydrophobic surfaces (Rothstein 2010; Cierpka et al. 2015; Lee et al. 2016), or to understand the function of endothelial cells, or for protective action against various vascular diseases (Rossi et al. 2009; Conway et al. 2013; Booth et al. 2014; Shemesh et al. 2015). For precise measurement of the wall shear stress, the wall surface information is very essential to determine the velocity gradient. However, the precise determination of surface position over the structured or complicated configuration like superhydrophobic surfaces or biological cells is very difficult. Sugii (2010) and Rossi et al. (2009, 2010) overcame this difficulty by combining the micro-PIV (μPIV, Lindken et al. 2009) with a focal plane-scanning system to obtain both the shear stress distribution and 3D shape of cells which were cultured inside the microchannels. However, in such cases, highly accurate positioning systems and a thin focal plane are necessary to obtain the 3D velocity fields because μPIV is a two-dimensional and two-component (2D2C) velocity measurement technique; therefore, velocity fields in different depth positions are required to reconstruct the 3D velocity field. Another method applicable to the structured wall is the digital holography microscopy (DHM), which can measure the 3D flow field (Katz and Sheng 2010). This technique can be used to determine the location of 3D particles and their velocity volumetrically; however, interferences of hologram occur at near-wall regions where the channel wall contains microstructures due to the difference in the refractive index between the structure and the fluid. Usually, such problems are overcome by matching the refractive indices of the fluids and the structured surfaces, but sometimes the index matching fluids limit the applications because of their high toxicity and concentration (for example, high concentration of NaI solution) (Talapatra and Katz 2012; Bocanegra Evans et al. 2016).

Recently, an astigmatism particle tracking velocimetry (APTV) has been proposed for obtaining the 3D3C velocity using single-view imaging (Cierpka et al. 2010, 2011, 2013). The APTV technique is a scan-free, low-cost, and easy technique for the 3D flow field measurement. APTV exploits the distortion of fluorescent particle images—that is induced when the particles are out of focal plane—by placing a cylindrical lens (CL) in front of the image sensor. Because the magnitude of the distortion of the particle image depends on the distance between the location of the particle and the focal plane of the objective lens, it becomes possible to obtain the 3D3C velocity in a measurement volume in a single-viewing by tracking each particle whose depth location can be calculated from the distortion. In previous studies, Cierpka et al. (2010) utilized the APTV to the laminar flow channel measurement and obtained the cross-sectional velocity distribution precisely. Additionally, the 3D configuration of an electrothermal microvortex and AC electroosmotic flows in microchannel were visualized

by APTV (Kumar et al. 2011; Liu et al. 2014, 2015). In contrast to the confocal μPIV (Kinoshita et al. 2006) and scanning stereoscopic μPIV (Lindken et al. 2006) which can also measure the 3D velocity, the APTV technique does not require scanning.

In this study, using the APTV technique, we demonstrate a measurement of a flow field and the wall shear stress distribution over the structured surface which has a circular micropillar array in a microfluidic channel. In addition, the measured results were compared with a numerical simulation. Recently, understanding the flow through porous media becomes a focused topic for the both life science and industrial application, for example, bacterium attachment, biofilm deformation, colloidal dispersion, oil recovery and so on (Valiei et al. 2012; Gunda et al. 2013; Debnath et al. 2017). In such studies, the micropillar array is used as an alternative to the porous media. Additionally, other studies which investigate the phenomena such as wetting and wicking (Saha et al. 2009; Luo and Xian 2014; Texier et al. 2016), particle and cell sorting (Sajeesh and Sen 2014), and drag reduction (Schäffel et al. 2016; Kim and Rothstein 2017) also used micropillar array. Although these studies suggest that the flow measurement around the micropillar array is of significant importance, the detailed information about flow field around the micropillar is still lacking. Recently, Bocanegra Evans et al. (2016) investigated flow fields in a microchannel with a micropillar array by DHM and obtained the 3D flow configuration and apparent wall shear stress distribution above the pillars. However, the flow measurement between the pillars was not achieved because the tracer particle concentration in their study was not sufficient for their PIV-based analysis method. To extend the knowledge put forward by Bocanegra Evans et al. (2016) further, we investigate the details of the entire flow field around the pillars and the wall shear stress distribution at the bottom wall of the channel using the APTV technique. Our observation would be helpful to understand the influence of microstructures in microchannels on 3D fluid structures and the wall shear stress distribution on the channel surface.

2 Experimental system

2.1 Experimental setup

A schematic of the APTV system used in this study is shown in Fig. 1. This system is the same as used in our previous study (Ichikawa et al. 2017). All optical elements and the imaging system are contained in an inverted microscope (ECLIPSE Ti-S, Nikon). To capture the distorted particle images, a 20× objective lens (NA 0.45, CFI S Plan Fluor ELWD 20×, Nikon) and a scientific CMOS (sCMOS) camera (960×720 pixels, 45 fps, ORCA-Flash 2.8, Hamamatsu
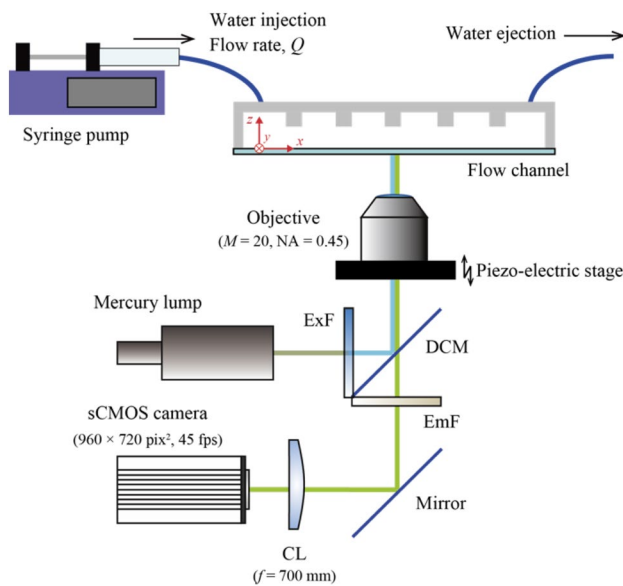
Fig. 1 Schematic of the APTV system. All setup is built in an inverted microscope

Photonics) were used. Pixel size of the imaging sensor on the camera is 3.63 μm × 3.63 μm and we used the binning mode of the camera. Therefore, the spatial resolution of the image corresponded to 0.363 μm/pixel. As an illumination source, a mercury lamp (Intensilight C-HGFI, Nikon) was used. To generate the distortion of the astigmatism, a CL of focal length $f = 700$ mm was placed in front of the imaging sensor of the camera. As the working fluid, ultrapure water (Direct-Q, Merck Millipore) that contains fluorescent polystyrene particles (1 μm in diameter, FluoSpheres, life technologies) as tracer particles was infused into the flow channel using a syringe pump (Pump 11 Elite, Harvard). The flow rate Q was controlled using the syringe pump. In this study, we used a microchannel which has a circular pillar array whose 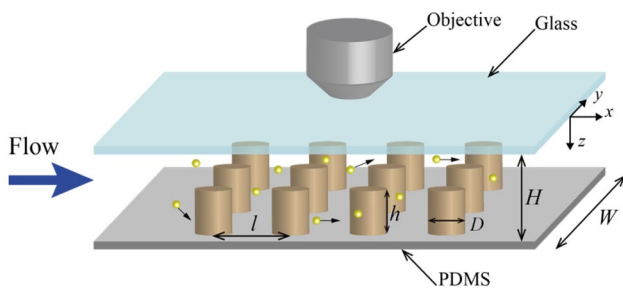geometry is shown in Fig. 2. The streamwise, spanwise, and depth directions correspond to x, y, and z axes, respectively. The upper side of the channel with the pillar array was made from PDMS (polydimethylsiloxane) and fabricated using the standard soft lithography technique. The bottom of the channel was made of a 1-mm-thick glass slide. The measurement area was sufficiently far from the inlet (approximately 10 mm) where the flow is fully developed.

2.2 Calibration of the particle location and the velocity measurement accuracy

The depth position of tracer particles in the microchannel can be determined from a distorted feature of the particle images. As shown in Fig. 3, the shape of the particle images is distorted transversely when particles locate closer to the imaging sensor than the focal point of the objective lens, and it is distorted longitudinally when the particles locate beyond the focal point. In this study, a calibration which correlates the degree of the distortion in the elliptical image and the depth position of a particle was conducted. In the calibration procedure, images of particles, which attached on glass wall and surrounded by water, were obtained with a 0.78 μm span in depth direction by scanning the objective lens using a piezo-electric stage as shown in Fig. 4. As the degree of the distortion, we employed Eq. (2) (Nishiwake and Motosuke 2014; Ichikawa et al. 2015):

$$F = a_y^2 - a_x^2. \tag{2}$$

Here, a_x and a_y are width and height of the distorted particle image, respectively (Fig. 3), and $|F|$ is equal to the square of the length between two focal points of the ellipse. The calibration curve between scanning distance z_{trv} and F is depicted in Fig. 5. In Fig. 5, the influence of the refractive

Fig. 2 Schematic of the microchannel made of PDMS and glass plate having dimensions $H = 40$ μm in height and $W = 2$ mm in width. One side of the channel has an array of circular pillars of diameter $D = 50$ μm and height of $h = 20$ μm. The pitch l between the pillars is 100 μm. The small spheres represent the tracer particles with a diameter of 1 μm
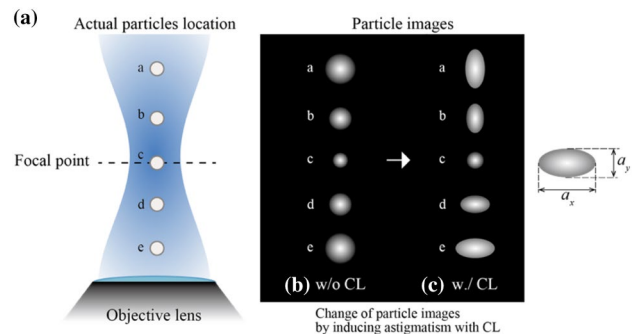

Fig. 3 Schematic of astigmatic particle imaging. **a** The actual particle location and the dashed line indicates the focal point of the objective lens. **b** The particle images without cylindrical lens. The particles a, b, d and e are on off-focus point and they are defocused. **c** The particle image is distorted elliptically according to the depth position using a cylindrical lens. The width and height of the distorted particle are defined as a_x and a_y, respectively
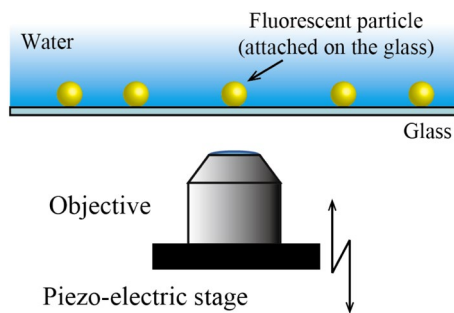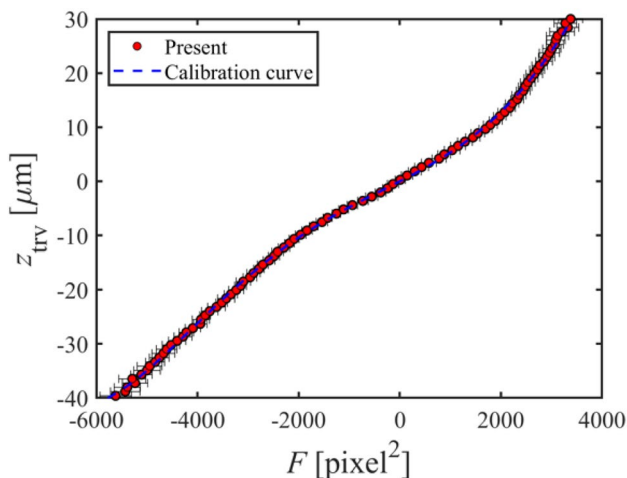
Fig. 4 Schematic of the calibration

Fig. 5 Calibration curve for the depth position of particles correlated with the degree of distortion F by Eq. (2) at each z position

index of water ($n = 1.333$) is included at each plot. Error bars are corresponded to the standard deviation of F at each position. Here the fifth-order polynomial fitting was employed as the calibration function. The calibration curve indicates that the measurement depth of the system is larger than the height of the channel (40 μm). Therefore, it is possible to determine the velocity field in the entire depth direction in the channel (the measurement volume in this study was set as $348 \times 261 \times 40$ μm³). The resulting depth resolution was approximately 1 μm.

Before the flow measurement in the microchannel, as shown in Fig. 2, an evaluation of the calibration curve (Fig. 5) and the wall shear stress determination were performed by a measurement of the Poiseuille flow in a Hele-Shaw cell ($W = 2$ mm and $H = 30$ μm). A temporally and spatially averaged streamwise velocity component u distribution in z direction is shown in Fig. 6. As the velocity determination procedure, we utilized a particle tracking method devised by Ishida et al. (2012). The uncertainty on determining the center of mass of particle was up to ± 1 pixel ($= 0.363$ μm), thus the uncertainty of velocity u was
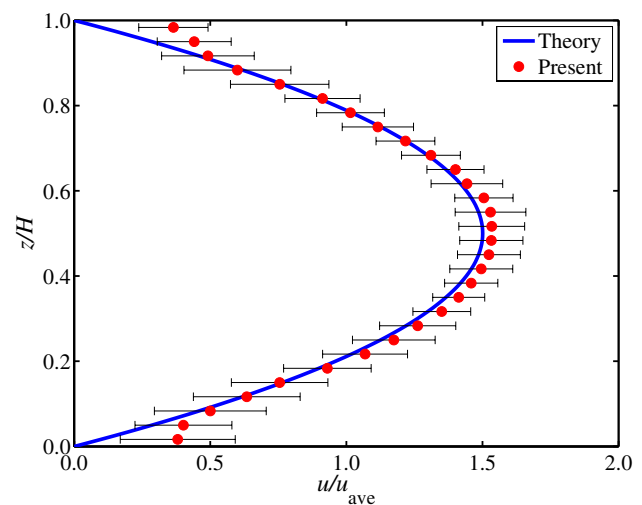

Fig. 6 Streamwise velocity distribution u/u_{ave} in a Hele-Shaw cell in depth direction obtained by the APTV. The channel geometry is $H = 30$ μm and $W = 2$ mm. The flow rate is $Q = 15$ μL/h. The theoretical calculations are also shown

within ± 16.5 μm/s by considering the frame rate of camera (45 fps). Here, the Reynolds number Re was 4.2×10^{-3} based on the hydraulic diameter of the channel D_h ($= 2WH/(W + H)$) of 29.6 μm and the cross-sectionally averaged velocity u_{ave} of 69.4 μm/s ($Q = 15$ μL/h). Error bars in the diagram correspond to the standard deviation of the velocity component u normalized by u_{ave} at each z location. Also, the height location z was normalized by H. Moreover, the measured u value was compared with that from theoretical calculation. The theoretical u of the two-dimensional Poiseuille flow is described as follows:

$$u_{theory} = \frac{6}{H^2 W} Q \left(z - \frac{z^2}{H} \right). \tag{3}$$

The experimental u/u_{ave} showed good agreement with the theoretical calculation (Fig. 6). At the near-wall location ($z/H < 0.07$ and $0.93 < z/H$), the measured values did not correspond to the theory. This could be due to the bias error caused by the particle–wall interaction (Goldman et al. 1967; Li and Yoda 2008; Kikuchi and Mochizuki 2015). In this study, u of $0.07 \leq z/H \leq 0.93$ was employed for the wall shear stress determination. The wall shear stress was calculated using Eq. (1) based on the measured u, excluding the near-wall region. This calculation agreed well with the theoretical value, within a $\pm 5\%$ uncertainty.

2.3 Numerical simulation for comparison

To consolidate the velocity components obtained in the present experiment, 3D numerical simulations were conducted. In Fig. 7, the calculation domain in the present simulation
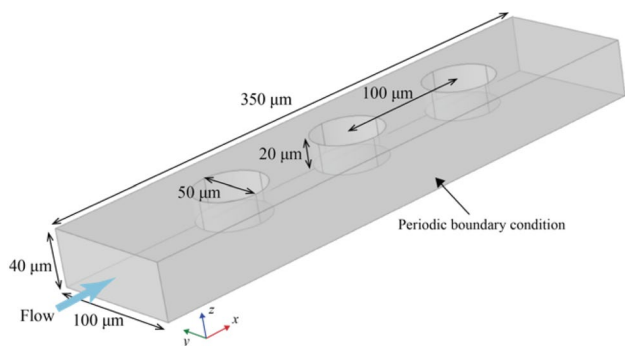
Fig. 7 Schematic of the domain based on the flow channel shown in Fig. 2 for the numerical calculation by COMSOL Multiphysics®

is illustrated. In this study, three pillars aligned in series were considered and the periodic boundary condition was applied in the y-direction. Additionally, the no-slip boundary condition was applied except for the inlet and outlet. As the computational grid, unstructured grid was utilized and the number of the grid is approximately 1.2×10^6 and the averaged volume of mesh is $1.23~\mu m^3$. The mass conservation equation and the Navier–Stokes equation without the inertia term (Stokes approximation) for isothermal and incompressible fluid are applied as the governing equations, as follows:

$$\nabla \cdot \mathbf{u} = 0, \tag{4}$$

$$-\nabla p + \mu \nabla^2 \mathbf{u} = 0, \tag{5}$$

where $\mathbf{u}$ is the velocity vector, p is the liquid pressure, and μ is the viscosity of the working fluid. The Reynolds number Re was set sufficiently small to satisfy the Stokes approximation. To solve these equations under the calculation domain shown in Fig. 7, a finite-element software package COMSOL Multiphysics® was utilized.

3 Results and discussion

3.1 Velocity distribution around the circular pillars

The flow field around nine pillars (3×3 units, as shown in Fig. 8a) at the channel center was measured. Then we summated the velocity information of the nine units for its symmetry (Fig. 8b, c). In this measurement, the flow rate Q was set at $Q = 30~\mu L/h$, and 15,000 frames were recorded with 45 fps. Here, the Reynolds number Re was 8.14×10^{-3} based on the hydraulic diameter $D_h = 78.4~\mu m$ and $u_{ave} = 104~\mu m/s$. The velocity distribution of each component, u, v, and w—normalized by the maximum value of each component—is depicted in Fig. 9. The extracted location of u and v corresponds to the plane of $x = 50~\mu m$, and that of w corresponds to the plane of $z = 19~\mu m$, respectively. Although a certain amount of scattering in the measured values were observed, the variation of the velocity due to the existence of the pillar could be confirmed in each velocity component. In this study, velocity data at each particle location were rearranged on grid points. The interpolated and rearranged velocity distributions after a post-processing are depicted in Fig. 9. As a post-processing, we utilized the procedure which is called an inverse distance rearrangement (Ido and Murai 2006) by using the weighting function based on the Gaussian function suggested by Agüí and Jiménez (1987). The grid interval is $5.0~\mu m \times 1.8~\mu m \times 1.8~\mu m$ ($x \times y \times z$). In the rearrange procedure, there was no overlap at each grid and an average of 13 particles contributed to the velocity of one grid point. From the results, it is confirmed that the velocity u component between the pillars in the spanwise direction becomes larger than that between the bottom wall and the tip of the pillar. This is due to the circumventing motion of the flow from the pillar. Therefore, the value of
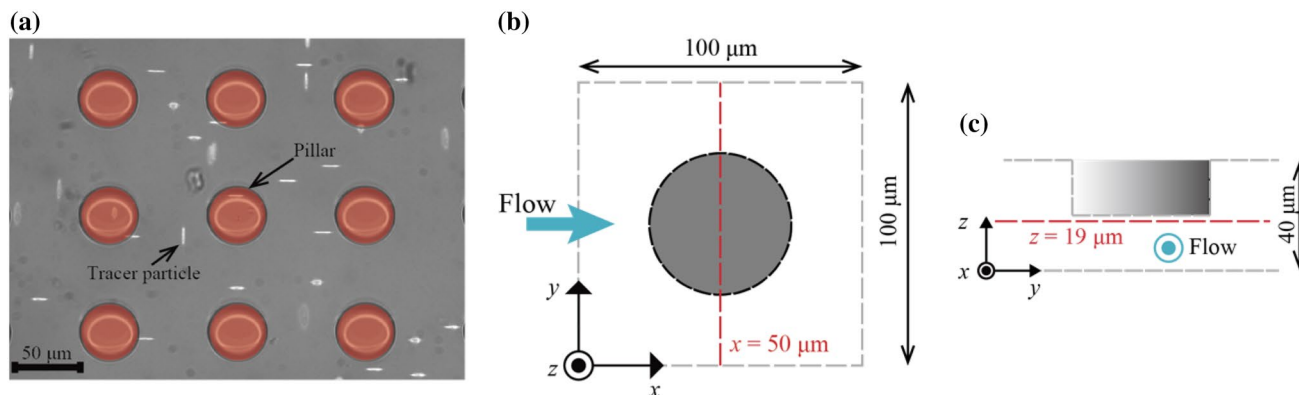

Fig. 8 Measurement location in the microchannel. **a** The red-hatched circles correspond to the circular pillars and the elliptically distorted images are the tracer particles. Velocity determination domain and coordinate systems around a pillar in **b** x–y plane and **c** y–z plane
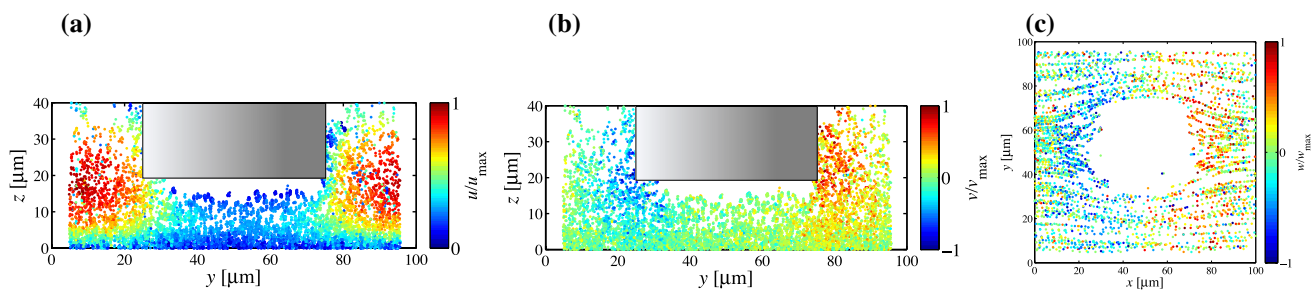
(a) **(b)** **(c)**

Fig. 9 Summated velocity component **a** u distribution and **b** v distribution at $x = 50$ μm (flow direction is perpendicular to the paper); **c** w distribution in the x–y plane at $z = 19$ μm (flow direction is from left to right). The extracted locations are indicated in Fig. 8
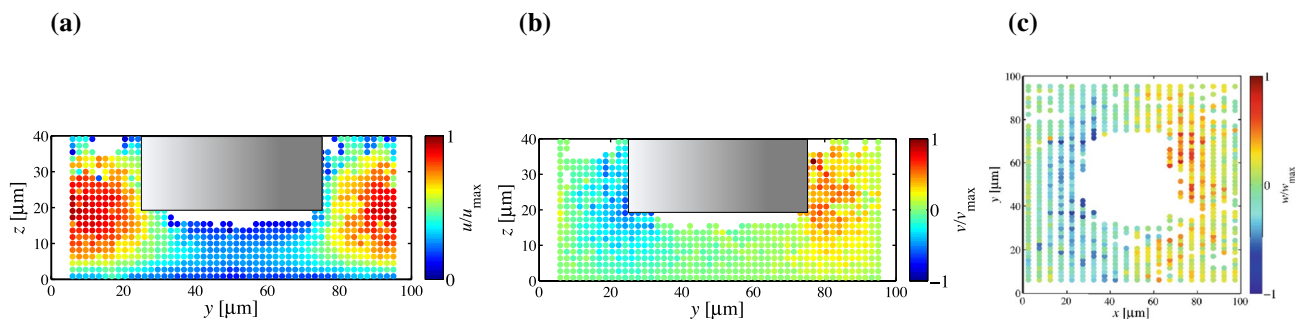

(a) **(b)** **(c)**

Fig. 10 Velocity component **a** u (flow direction perpendicular to the paper), **b** v (flow direction perpendicular to the paper), and **c** w (flow direction from left to right) distribution after rearrangement to grid points from the distribution shown in Fig. 9

velocity v component of the left and right side of the figure shows the difference. As the coordinate system is defined as Fig. 8b, c, the value of v of left side of Fig. 10b becomes $v < 0$ μm/s. On the other hand, on right side of Fig. 10b, v becomes $v > 0$ μm/s. Moreover, in z direction, the flow has downward and upward components at upstream and downstream of the pillar, respectively, to bypass the pillar. In the w-component distribution, a different behavior from the previous study was observed. According to Bocanegra Evans et al. (2016), the flow motion slows down before encountering a pillar and lifts as it passes the pillars directed toward the next pillar downstream. Additionally, these researchers mentioned that the flow field over the pillar array shows high three-dimensionality. On the other hand, in our study, streamline is attached along with the pillar canopy as shown in Fig. 11. From this fact, it is suggestive that the channel geometry, especially the distance between the tip of the pillar and the bottom wall surface (H–h) and the distance between each pillar would affect the fluid motion in the z direction.

For comparison with the measurement results, the calculation results around the domain of the center pillar were extracted. The results of the numerical simulation are shown in Fig. 12. Compared with Figs. 9 and 10, Fig. 12 shows qualitatively similar velocity distribution to the experimental results. Therefore, interpolated velocity distributions
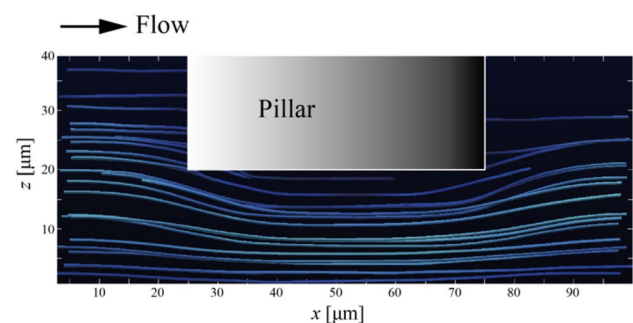

Fig. 11 Streamline in the x–z plane around the pillar center ($40 \leq y \leq 60$ μm)

obtained by APTV seem acceptable and this implies that it is possible to determine the wall shear stress distribution based on these velocity distributions.

3.2 Wall shear stress distribution determination

Subsequently, we calculated the wall shear stress τ_w distribution from the velocity distribution obtained in the previous section. Before determining τ_w empirically, we confirmed that the distribution obtained by the numerical simulation and the velocity component u is dominant over v and w for the τ_w calculation in terms of the channel we used. For the
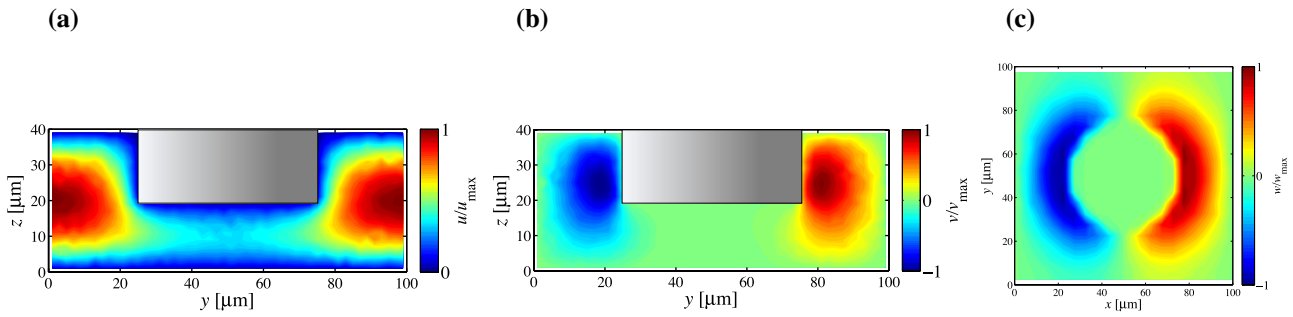
Fig. 12 Numerical calculation results of velocity component **a** u (flow direction perpendicular to the paper), **b** v (flow direction perpendicular to the paper), and **c** w (flow direction from left to right) distributions at the location indicated in Fig. 8b, c

determination of wall shear stress for x direction, $\tau_{w,x}$ by Eq. (1), velocity gradient du/dz based on u distribution in z direction was determined at each x–y location by a second-order polynomial fitting. The wall location was assumed as the point where the local velocity component u becomes zero (Sugii 2010; Rossi et al. 2009). Using these procedures, the wall shear stress $\tau_{w,x}$ distributions at the lower and the upper wall of the microchannel were obtained, respectively, as shown in Fig. 13. The spatial resolution of $\tau_{w,x}$ is 5.0 μm × 1.8 μm (x × y). These distributions were normalized by the maximum value $\tau_{w,x_{max}}$. From Fig. 13, it is confirmed that on both upper and bottom surfaces, the high wall shear stress area exists beside the pillar and it corresponds to the high velocity region. According to the previous study by Bocanegra Evans et al. (2016), when H–h becomes very large, the influence of the pillar on the velocity distribution near the opposite wall (wall which does not contain a pillar array) diminishes and the shear stress on that wall will be uniform. On the other hand, in this study, it was observed that the wall shear stress is not uniform on the opposite side

(flat wall). From this fact, it is indicated that it is possible to induce the non-uniform wall shear stress distribution on both upper and lower channel walls if the pillar array is set to one side of the wall to satisfy a sufficiently small H–h. Comparisons of the maximum and minimum wall shear stress in a flat channel, which has the same H and W ($\tau_{w_{flat}} = 15.7$ mPa), was performed. As a result, it was found that the maximum $\tau_{w,x}$ was 1.24 times as large as $\tau_{w_{flat}}$ and the minimum $\tau_{w,x}$ was 0.25 times as small as $\tau_{w_{flat}}$ at the bottom side of the wall (no pillars), respectively. Moreover, on the pillar array side, the maximum $\tau_{w,x}$ was $1.16\tau_{w_{flat}}$ and the minimum $\tau_{w,x}$ was $0.2\tau_{w_{flat}}$, respectively. These results indicate that the change of the wall surface shape can induces a drastic change of the wall shear stress distribution.

The result shown in Fig. 13 was also compared with the numerical simulation shown in Fig. 14. Although the experimentally obtained shear stresses show some dispersions, it is confirmed that both results show qualitatively good agreement. The dispersion is possibly due to the error in the velocity determination and the roughness of the grid interval
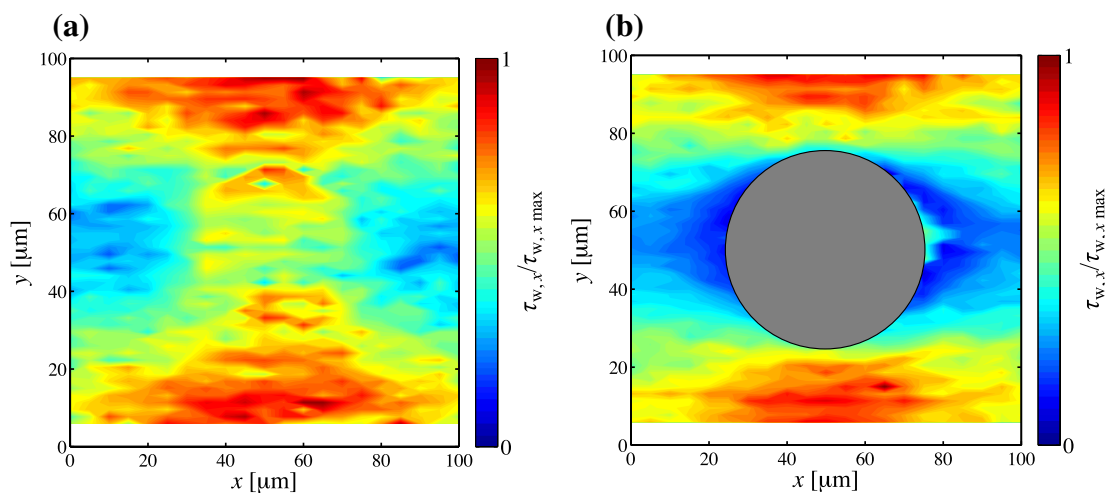

Fig. 13 Wall shear stress $\tau_{w,x}$ distribution based on the empirically obtained velocity component u distribution using the APTV technique at **a** the lower side of the channel and **b** the upper side of the channel
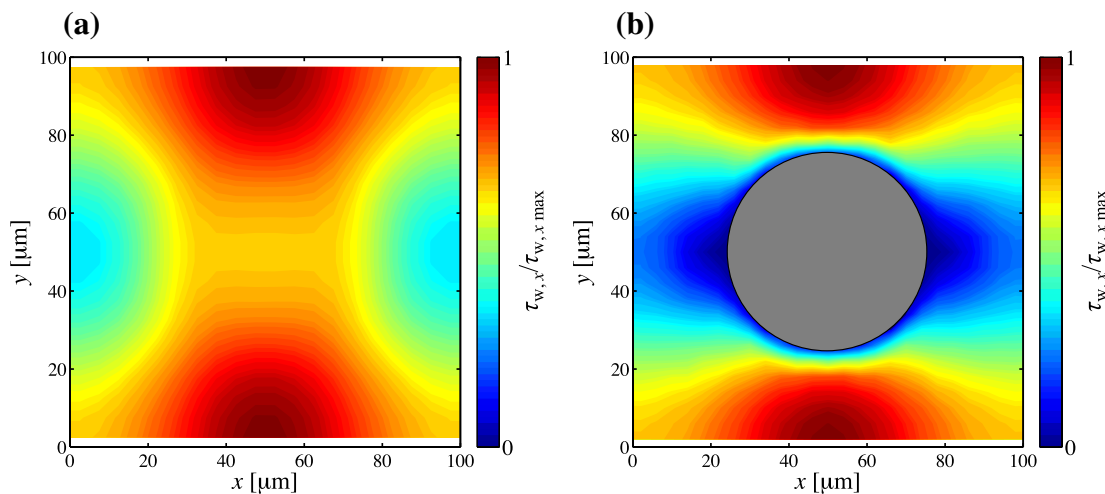
Fig. 14 Numerical calculation results of the wall shear stress $\tau_{w,x}$ distribution normalized by the maximum value $\tau_{w,x_{max}}$ at **a** the lower wall of the channel, and **b** the upper wall of the channel

in x direction. From this fact, in contrast to the conventional µPIV technique for wall shear stress determination, the scan of the focal plane in the flow fields in the depth direction for the velocity gradient acquisition was not required and we achieved shear stress measurement easily and quickly using the APTV technique. Therefore, it is confirmed that the APTV technique is valid for wall shear stress measurement in microchannels with micron resolution.

4 Conclusions

In this study, a measurement of 3D velocity distribution and wall shear stress $\tau_{w,x}$ distribution in a microchannel having a circular pillar array was conducted using the APTV technique. In the measurement, the variations of the velocity and $\tau_{w,x}$ attributable to the existence of the pillars were observed, and it was confirmed that the wall shear stress between the pillars in the spanwise direction is larger than the other area in this channel, and the location corresponds to where the velocity component u is large. In addition, it was confirmed that the shear stress distribution on both the upper and lower walls can be modified or modulated when the space between the tip of the pillar and the opposite wall is small (for example, the space is comparable to the height of the pillar, 20 µm in this study). From these facts, the influence of the micropillar array on the velocity field and shear stress on the channel surface was evident. Furthermore, we confirmed that empirically obtained velocity distribution and $\tau_{w,x}$ distribution showed good agreements with numerical simulation results. Although it is necessary to improve velocity measurement for more accurate $\tau_{w,x}$ distribution determination, it is considered that the effectiveness of $\tau_{w,x}$ determination

as distribution with micron resolution by the APTV was indicated. These results suggested the potential of APTV as the valid technique for understanding flow–structure or flow–cell interaction in a µTAS or lab-on-a-chip platforms.

References

Agüí CJ, Jiménez J (1987) On the performance of particle tracking. J Fluid Mech 185:447–468

Amini H, Sollier E, Masaeli M, Xie Y, Ganapathysubramanian B, Stone HA, Di Carlo D (2013) Engineering fluid flow using sequenced microstructures. Nat Commun 4:1826

Blossey R (2003) Self-cleaning surfaces-virtual realities. Nat Mater 2:301–306

Bocanegra Evans H, Gorumlu S, Aksak B, Castilo L, Sheng J (2016) Holographic microscopy and microfluidics platform for measuring wall stress and 3D flow over surfaces textured by micro-pillars. Sci Rep 6:28753

Booth R, Noh S, Kim H (2014) A multiple-channel, multiple-assay platform for characterization of full-range shear stress effects on vascular endothelial cells. Lab Chip 14:1880–1890

Cierpka C, Segura R, Hain R, Kähler CJ (2010) A simple single camera 3C3D velocity measurement technique without errors due to depth of correlation and spatial averaging for microfluidics. Meas Sci Technol 21:045401

Cierpka C, Rossi M, Segura R, Kähler CJ (2011) On the calibration of astigmatism particle tracking velocimetry for microflows. Meas Sci Technol 22:015401

Cierpka C, Lütke B, Kähler CJ (2013) Higher order multi-frame particle tracking velocimetry. Exp Fluids 54:1533

Cierpka C, Rossi M, Kähler CJ (2015) Wall shear stress measurement. In: Li D (ed) Encyclopedia of microfluidics and nanofluidics, 2nd edn. Springer, New York, pp 3479–3486

Conway DE, Breckenridge MT, Hinde E, Gratton E, Chen CS, Schwartz MA (2013) Fluid shear stress on endothelial cells modulates mechanical tension across VE-cadherin and PECAM-1. Curr Biol 23:1024–1030

Debnath N, Hassanpourfard M, Ghosh R, Trivedi J, Thundat T, Sabrzadeh M, Kumar A (2017) Abiotic streamers in a microfluidic system. Soft Matter 13:8698–8705

Elvira KS, i Solvas XC, Wootton RCR, deMello AJ (2013) The past, present and potential for microfluidic reactor technology in chemical synthesis. Nat Chem 5:905–915

Goldman AJ, Cox RG, Brenner H (1967) Slow viscous motion of a sphere parallel to plane wall-1 Motion through a quiescent flow. Chem Eng Sci 22:637–651

Gunda NSK, Joseph J, Tamayol A, Akbari M, Mitra SK (2013) Measurement of pressure drop and flow resistance in microchannels with integrated micropillars. Microfluid Nanofluid 14:711–721

Ichikawa Y, Nishiwake K, Wakayama H, Kameya Y, Yamamoto M, Motosuke M (2015) Three-dimensional measurement of near-wall velocity in millimeter channel by a single view imaging. In: Proceedings of the ASME 2015 international technical conference and exhibition on packaging and integration of electronic and photonic microsystems and ASME 2015 13th international conference on nanochannels, microchannels, and minichannels (InterPACK/ICNMM2015) 2015, San Francisco, USA

Ichikawa Y, Yamamoto K, Yamamoto M, Motosuke M (2017) Near-hydrophobic-surface flow measurement by micro-3D PTV for evaluation of drag reduction. Phys Fluids 29:092005

Ido T, Murai Y (2006) A recursive interpolation algorithm for particle tracking velocimetry. Flow Meas Instrum 17:267–275

Ishida A, Toki H, Motosuke M, Honami S (2012) Particle accumulation by AC electroosmosis in microfluidic device with co-planar electrodes. J Themal Sci Technol 7:475–486

Katz J, Sheng J (2010) Applications of holography in fluid mechanics and particle dynamics. Annu Rev Fluid Mech 42:531–555

Kikuchi K, Mochizuki O (2015) Velocity profile of thin film flows measured using a confocal microscopy particle image velocimetry system with simultaneous multi depth position. Meas Sci Technol 26:025301

Kim JH, Rothstein JP (2017) Role of interface shape on the laminar flow through an array of superhydrophobic pillars. Micrfluid Nanofluid 21:78

Kinoshita H, Kaneda S, Fujii T, Oshima M (2006) Three-dimensional measurement and visualization of internal flow of a moving droplet using confocal micro-PIV. Lab Chip 7:338–346

Kumar K, Cierpka C, Williams SJ, Kähler CJ, Wereley ST (2011) 3D3C velocimetry measurements of an electrothermal micro-vortex using wavefront deformation PTV and a single camera. Microfluid Nanofluid 10:355–365

Lee C, Choi CH, Kim CJ (2016) Superhydrophobic drag reduction in laminar flows: a critical review. Exp Fluids 57:176

Li HF, Yoda M (2008) Multilayer nano-particle image velocimetry (MnPIV) in microscale Poiseuille flows. Meas Sci Technol 19:075402

Lindken R, Westerweel J, Wieneke B (2006) Stereoscopic micro particle image velocimetry. Exp Fluids 41:161–171

Lindken R, Rossi M, Große S, Westerweel J (2009) Micro-particle image velocimetry (µPIV): recent developments, applications, and guidelines. Lab Chip 9:2551–2567

Liu Z, Speetjens MFM, Frijns AJH, van Steenhoven AA (2014) Application of astigmatism µ-PTV to analyze the vortex structure of AC electroosmotic flows. Microfluid Nanofluid 16:553–569

Liu Z, Frijns AJH, Speetjens MFM, van Steenhoven AA (2015) Particle focusing by AC electroosmosis with additional axial flow. Microfluid Nanofluid 18:1115–1129

Luo C, Xian M (2014) Existence and stability of an intermediate wetting state on circular micropillars. Microfluid Nanofluid 17:539–548

Nishiwake K, Motosuke M (2014) A simple 3D3C velocimetry in microscale using single camera based on anisotropic defocus method. In: Proceedings of 16th international symposium on flow visualization (ISFV16) 2014, Okinawa, Japan

Rossi M, Lindken R, Hierck BP, Westerweel J (2009) Tapered microfluidic chip for the study of biochemical and mechanical response at subcellular level of endothelial cells to shear flow. Lab Chip 9:1403–1411

Rossi M, Lindken R, Westerweel J (2010) Optimization of multiplane µPIV for wall shear stress and wall topography characterization. Exp Fluids 48:211–223

Rothstein JP (2010) Slip on superhydrophobic surfaces. Annu Rev Fluid Mech 42:89–109

Saha AA, Mitra SK, Tweedie M, Roy S, McLaughlin J (2009) Experimental and numerical investigation of capillary flow in SU8 and PDMS microchannels with integrated pillars. Microfluid Nanofluid 7:451–465

Sajeesh P, Sen AK (2014) Particle separation and sorting in microfluidic devices: a review. Microfluid Nanofluid 17:1–52

Schäffel D, Koynov K, Vollmer D, Butt HJ, Schönecker C (2016) Local flow field and slip length of superhydrophobic surfaces. Phys Rev Lett 116:134501

Shemesh J, Jalilian I, Shi A, Yeoh GH, Tate MLK, Warkiani ME (2015) Flow-induced stress on adherent cells in microfluidic devices. Lab Chip 15:4114–4127

Stoecklein D, Wu CY, Owsley K, Xie Y, Di Carlo D, Ganapathysubramanian B (2014) Micropillar sequence designs for fundamental inertial flow transformations. Lab Chip 14:4197–4204

Stone HA, Stroock AD, Ajdari A (2004) Engineering flows in small devices: microfluidics toward a lab-on-a-chip. Annu Rev Fluid Mech 36:381–411

Stroock AD, Dertinger SKW, Ajdari A, Mezic I, Stone HA, Whitesides GM (2002) Chaotic mixer for microchannel. Science 295:647–651

Sugii Y (2010) Simultaneous measurement of wall shear stress distribution and three-dimensional shape of living endothelial cells cultured in microchannel. J Biomech Sci Eng 5:625–634

Talapatra, Katz J (2012) Coherent structures in the inner part of a rough-wall channel flow resolved using holographic PIV. J Fluid Mech 711:161–170

Texier BD, Laurent P, Stoukatch S, Dorbolo S (2016) Wicking through a confined micropillar array. Microfluid Nanofluid 20:53

Toner M, Irimia D (2005) Blood-on-a-chip. Annu Rev Biomed Eng 7:77–103

Valiei A, Kumar A, Mukherjee PP, Liu Y, Thundat T (2012) A web of streamers: biofilm formation in a porous microfluidic device. Lab Chip 12:5133